RSC Advances

ROYAL SOCIETY OF CHEMISTRY

www.rsc.org/advances

Theoretical study on the influence of a secondary metal on the Cu(110) surface with the presence of H_2O for methanol decomposition

Yong-Chao Zhang[1]，Rui-Peng Ren[1]，Shi-Zhong Liu[2]，Zhi-Jun Zuo[1]* and Yong-Kang Lv[1]*

[1]Key Laboratory of Coal Science and Technology of Ministry of Education and Shanxi Province, Taiyuan University of Technology, Taiyuan 030024, Shanxi China; [2] Department of Chemistry, Stony Brook University, Stony Brook, New York 11794, United States

***Corresponding author. Fax: +86 351 6010386. E-mail address: lykang@tyut.edu.cn (Y.-K. Lv); zuozhijun@tyut.edu.cn (Z.-J. Zuo).**

Abstract: Density functional theory calculations with the continuum solvation slab model are performed to investigate the effect of metal dopants on the Cu(110) surface with the presence of H_2O for the methanol decomposition. The sequential dehydrogenation of methanol ($CH_3OH \rightarrow CH_3O \rightarrow CH_2O \rightarrow CHO \rightarrow CO$) is studied in present work. The results show that the introduction of different metals (Pt, Pd, Ni, Mn) on the H_2O/Cu(110) surface notably influence on the adsorption configurations and adsorption energies of all adsorbates, and remarkably affect the reaction energies and activation energies of the elementary steps. The Pt, Pd and Ni doped H_2O/Cu(110) surface are able to promote the hydrogen production from methanol decomposition, but Mn doped H_2O/Cu(110) surface is unfavorable for the reaction. The activity of methanol decomposition decreases in the follow: Pd-H_2O/Cu(110) > Pt-H_2O/Cu(110) > Ni-H_2O/Cu(110) > H_2O/Cu(110) > Mn-H_2O/Cu(110). Finally, the Brønsted-Evans-Polanyi plot for the main methanol dissociation steps on the metal doped and un-doped H_2O/Cu(110) surfaces are identified, and a linear relationship between the reaction energies and transition state energies is obtained.

Keywords: DFT; methanol decomposition; metal dopants; H_2O/Cu(110); BEP

1. Introduction

Nowadays, the worldwide energy consumption is still mainly on fossil fuels [1], but the excessive consumption of fossil fuels has caused climate change [2, 3] due to a huge amount of greenhouse gas emissions, that damaged our planet's ecosystem to some extent [4]. In order to meet the world's energy demand and improve the adverse environmental conditions, there is an urgency to explore alternative and environmentally-friendly energy resources. As an ideal fuel, more recently, hydrogen energy is receiving more and more attention because water is the sole by-product [5]. However, the intrinsic physical properties of hydrogen [6, 7] make it not an ideal energy media. Methanol can be used as a material for the storage of hydrogen [8-11], owing to the high energy density and H/C ratio, the absence of C-C bond, abundant and low-cost source as well as safer and more convenient to a long distance transportation.

Methanol decomposition ($CH_3OH \rightarrow 2H_2+CO$ ΔH^o_{298K}= 90.7 KJ/mol) is an effective method for hydrogen production. Numerous efforts are devoted to understanding the mechanism of methanol decomposition on various metal surfaces, especially on transition metal catalysts[12-22]. The Cu based catalysts are widely used in hydrogen production from methanol due to the unique catalytic activity and selectivity[15-17]. However, during the reaction, the catalyst is easily suffering from the problem of thermal instability due to severe metal coking and sintering[23]. To improve the catalytic performance and reduce the reaction temperature, substantial efforts are devoted to designing more effective catalysts. Bimetallic alloys are received extensively attention in heterogeneous

catalysis[24-37]. Due to their similar cell parameters and identical crystal structure, metallic Pt, Pd and Ni with Cu can form Pt-Cu, Pd-Cu and Ni-Cu binary alloys. Previous literature reported that the Pt-Cu alloy are used in hydrocarbon reforming reaction[25] and the Pd-Cu, Ni-Cu bimetallic alloy catalyst presenting superior behavior for the steam reforming of methanol [33, 34]. In addition, the Cu-Mn spinel catalyst is used to the methanol steam reforming[35, 36]. Up to now, no experimental and theoretical are reported to understand the hydrogen formation from methanol decomposition on metal (Pt, Pd, Ni, Mn) doped Cu based catalysts, and to further explore the influence of metal dopant on the reaction. Therefore, our work would be important to clarify the influence of a secondary metal for methanol decomposition, what's more, to explore new methanol decomposition catalysts.

To the best of our knowledge, many heterogeneous catalytical processes occurred in a solvent environment for the purpose of dissolving the reactants, and then influence on the reaction rate and products selectivity [21, 38-40]. In the actual system for methanol decomposition, water or water vapor is almost never avoidable, and its influence on methanol dissociation needs to be deeply investigated. Unfortunately, few studies for heterogeneous catalysis which occurs on the solid/liquid interface are reported. Wang et al, Fang et al and Okamoto et al study the formic acid oxidation, methanol oxidation and the dehydrogenation of methanol on Pt(111) with the presence of water molecules [41-43]. Their research showed that the water molecules significantly affect the adsorption energies and activation energies of the corresponding adsorbates and elementary steps. In this work, water molecules are

added onto the solid surface to simulate the behavior of methanol decomposition on the solid/liquid interface environment.

Therefore, in the present study, by using the density functional theory (DFT), the methanol decomposition on the metal (Pt, Pd, Ni, Mn) doped and un-doped H_2O/Cu surfaces are investigated to understand the bimetallic effect on the reaction. To further elucidate the Kinetic-Thermodynamic relationships, Brønsted-Evans-Polanyi (BEP) plot is also carried out. The results are expected to reveal the mechanism of methanol decomposition on the metal doped Cu catalysts with the presence of water molecules. Furthermore, the calculation results may be useful for designing new catalytic materials for methanol decomposition reaction.

2. Computational models and methods

2.1. Surface model

For methanol decomposition, the real copper catalyst is modeled by the Cu(110) surface, and explicit four water molecules are added onto the Cu(110) surface as the first solvation shell to model the solvation environment.

The Cu(110) surface is cleaved from the face-centered cubic (fcc) crystal structure, and the lattice parameter of Cu is 3.615 Å, which is in agreement with the experimental values [44, 45]. From the optimized bulk structure, the Cu(110) surface is modeled using a four atomic layer slabs with a periodic p(3 × 3) unit cell, and 9 atoms at each layer. Meanwhile, a 15 Å thick vacuum gap is employed to separate the periodic images of the slab. In all calculations, the top two layers and adsorbates are allowed fully relaxed and the bottom two slab layers are fixed in their bulk position.

One surface Cu atom is substituted by a dopant (Pt, Pd, Ni, Mn) atom, and the corresponding dopant coverage is 1/9 ML. As shown in Fig.1(a) and (b), the structure of M-H_2O/Cu(110) (M: Pt, Pd, Ni, Mn) and un-doped H_2O/Cu(110) surfaces are used for the present calculation.

2.2. Calculation methods

The Kohn-Sham DFT calculation is performed using the Vienna ab initio simulation package (VASP) [46, 47] with the projector-augmented wave (PAW) pseudopotentials [48]. The generalized gradient approximation (GGA) with the Perdew, Burker and Ernzerhof (PBE) functional is used to treat the exchange-correlation energy [48-50]. The kinetic energy cutoff is 400 eV. A 3 × 3 × 1 Monkhorst-Pack k-point mesh with Monkhorst-Paxton smearing of 0.1 eV is sampled to the Brillouin zone [51]. The transition states (TS) and the minimum energy paths (MEP) are studied using the climbing-image nudged elastic band (CI-NEB) method [52] combined with the dimer method [53]. The TS is identified with imaginary frequencies through the vibrational analysis. The geometries structure is deemed converged until the forces of all relax atoms are less than 0.03 eV/Å, and the convergence of energy is set to 1×10^{-5} eV. The molecules in the gas phase are calculated using a 15×15×15 $Å^3$ cubic unit cell.

The adsorption energy (E_{ads}) is defined as:

$$E_{ads} = E_{(adsorbate+4H_2O)/slab} - E_{4H_2O/slab} - E_{adsorbate}$$

$E_{(adsorbate+4H_2O)/slab}$ is the total energy of the adsorbate on the metal (Pt, Pd, Ni, Mn) doped or un-doped H_2O/Cu(110) surface. $E_{4H_2O/slab}$ is the energy of the metal (Pt, Pd, Ni, Mn) doped or un-doped H_2O/Cu(110) surface. $E_{adsorbate}$ is the energy of the

adsorbate molecule in vacuum situation. Obviously, a negative E_{ads} value represents exothermic adsorption, and more negative values indicates the strong interaction between the adsorbates with the H_2O/Cu(110) surface.

3. Results and discussion

3.1. Reaction intermediates

The most stable adsorption configurations of the reaction intermediates on the metal (Pt, Pd, Ni, Mn) doped and un-doped H_2O/Cu(110) surfaces, which involves CH_3OH, CH_3O, CH_2O, CHO and CO, are shown in Fig.2. In addition, we have to mention that the reaction intermediates with the presence of water molecules can form hydrogen bond [42], which may facilitate the adsorption.

3.2. Reaction Mechanism

To our best knowledge, CH_3OH decomposition involves a series of elementary steps on the Cu catalysts [12, 13, 54-56]. According to the previous DFT reported [12, 13, 55-57], the C-H scission of methanol or intermediates during methanol decomposition is easier than that of C-O scission, and the sequential dehydrogenation steps of CH_3OH is the main route for CH_3OH decomposition, as follows: $CH_3OH \rightarrow CH_3O \rightarrow CH_2O \rightarrow CHO \rightarrow CO$. Therefore, in the following discussion, we will concentrate on the reactions between the main dehydrogenation products on the metal (Pt, Pd, Ni, Mn) doped H_2O/Cu(110) surfaces, and the results are compared with those obtained on the un-doped H_2O/Cu(110) surface. In all calculations, we use IS, TS and FS to represent the initial state, the transition state and the final state, respectively.

3.2.1 Pt-H_2O/Cu(110)

For the methanol decomposition on the Pt doped H_2O/Cu(110) surface, the potential energy diagram with the optimal pathway is shown in Fig.3. The initial step of the reaction ($CH_3OH \rightarrow CH_3O+H$) starts from the adsorbed CH_3OH, where the CH_3OH adsorbs on Pt through O with an adsorption energy of -38.58 KJ/mol. The dehydrogenation step through TS1 needs to overcome a barrier of 43.40 KJ/mol with exothermicity of -27.00 KJ/mol. The formation of CH_2OH via C-H bond scission from CH_3OH has an activation energy of 188.06 KJ/mol, which is higher than that of the CH_3O formation (43.40 KJ/mol), (see Fig S1 in the supporting information). The result indicates that the CH_3O formation from CH_3OH is easily to happen. The dehydrogenation of CH_3O is the next step and the CH_3O adsorbs on the Pt-Cu site with an adsorption energy of -277.75 KJ/mol. The CH_2O and H are generated during the CH_3O dissociation through TS2. The reaction ($CH_3O \rightarrow CH_2O+H$) has an activation energy of 49.18 KJ/mol with endothermicity of 15.43 KJ/mol. Immediately following, the further dehydrogenation of CH_2O to CHO, which is labeled as $CH_2O \rightarrow$ CHO+H. After optimization, the CH_2O adsorbs on the Pt-Cu site with C and O bind to Pt and Cu, respectively. The corresponding adsorption energy is -85.83 KJ/mol. After the TS3, the CHO and H are produced, and the reaction is exothermicity of -30.86 KJ/mol with an activation energy of 50.15 KJ/mol. The adsorption energy of CHO is -286.43 KJ/mol, where the CHO adsorbs on Pt through C. Subsequently, the dehydrogenation of CHO to CO ($CHO \rightarrow CO+H$) through TS4 is exothermic by -72.33 KJ/mol and needs to overcome a barrier of 60.76 KJ/mol.

3.2.2 Pd-H_2O/Cu(110)

On the Pd doped H_2O/Cu(110) surface, the potential energy diagram of the main route for CH_3OH decomposition is given in Fig.4. The reaction initiates by the dehydrogenation of the adsorbed CH_3OH to generate CH_3O and H through TS5. The stable adsorption structure of CH_3OH adsorbs on Pd via O with an adsorption energy of -50.15 KJ/mol. This reaction is endothermic of 6.75 KJ/mol with an activation energy of 19.29 KJ/mol. We also note that the CH_2OH formation needs to overcome a high barrier of 189.99 KJ/mol, which is higher than that of the CH_3O formation (19.29 KJ/mol). Similar to that of on the Pt doped H_2O/Cu(110) surface, the CH_2OH formation is unlikely to occur (the corresponding details are shown in Fig.S1 in the supporting information). Subsequently, the formed CH_3O further dehydrogenate to CH_2O via TS6, which has an activation energy of 41.47 KJ/mol with endothermicity of 12.54 KJ/mol. In this step, CH_3O strongly binds to the Pd-Cu site with an adsorption energy of -280.64 KJ/mol. After the TS6, the formed CH_2O adsorbs on the Pd-Cu site through C and O bind to Pd and Cu, respectively. The corresponding adsorption energy is -82.94 KJ/mol. The next step is the CHO formation through TS7. The dehydrogenation of CH_2O is energetically neutral with exothermic by -0.96 KJ/mol, and the activation energy is 39.54 KJ/mol. The final step is the CO production from the CHO→CO+H reaction via TS8. After optimization, The CHO adsorbs on Pt through C with an adsorption energy of -256.53 KJ/mol, and the formed CO binds to Pt through C. The calculated activation energy for this step is 57.86 KJ/mol, and the reaction is exothermic by -71.37 KJ/mol.

3.2.3 Ni-H_2O/Cu(110)

In the case of CH_3OH decomposition on the Ni doped H_2O/Cu(110) surface, the potential energy diagram of the main steps is presented in Fig.5. Similar to the case of CH_3OH dissociation on the Pt and Pd doped H_2O/Cu(110) surface, there are two possible paths for the initial CH_3OH dehydrogenation: O-H and C-H bond scission routes. For the reaction of $CH_3OH \rightarrow CH_3O+H$, after optimization, the CH_3OH adsorbs on Ni through O with an adsorption energy of -74.26 KJ/mol, and the CH_3O and H are generated through TS9. This step is moderately uphill, and needs to overcome a barrier of 92.58 KJ/mol with exothermicity of -44.36 KJ/mol. The formation of CH_2OH requires an activation energy of 169.73 KJ/mol, which is higher than that of the CH_3O formation (92.58 KJ/mol), (see Fig.S1). Therefore, the CH_3O formation is easy to occur. Subsequently, the formed CH_3O further dehydrogenate to CH_2O through TS10. In this step, the adsorbed CH_3O binds to Ni with an adsorption energy of -338.50 KJ/mol. The activation energy and reaction energy are 103.19 and 28.93 KJ/mol, respectively. The next step is CH_2O dissociation through TS11. In this process, the CH_2O adsorbs on Ni through both C and O with an adsorption energy of -130.19 KJ/mol. The reaction of the CHO and H production from CH_2O species is calculated to be exothermic by -23.15 KJ/mol with an activation energy of 62.69 KJ/mol. The last step for the stepwise dehydrogenation of CH_3OH on the Ni doped H_2O/Cu(110) surface is the CHO dissociation to CO via TS12, which is labeled as $CHO \rightarrow CO+H$. The most stable adsorption configuration of CHO binds to Ni through C, and the corresponding adsorption energy is -308.61 KJ/mol. This step is exothermic by -72.33 KJ/mol, and needs to overcome a barrier of 27.00 KJ/mol.

3.2.4 Mn-H_2O/Cu(110)

On the Mn doped H_2O/Cu(110) surface, the reaction coordinates for CH_3OH decomposition with the optimal pathway are depicted in Fig.6. Initially, CH_3OH adsorbs on Mn via O with an adsorption energy of -118.62 KJ/mol. The initial step of $CH_3OH \rightarrow CH_3O+H$ via TS13 has an activation energy of 26.04 KJ/mol, and the reaction energy is -91.62 KJ/mol. As another possible pathway, the CH_2OH formation is unlikely due to the high activation energy of 162.02 KJ/mol (see Fig.S1 in the supporting information). The following step is the dehydrogenation of CH_3O to CH_2O through TS14 with an activation energy of 123.44 KJ/mol, and the reaction is energetically neutral with endothermicity of 0.96 KJ/mol. In this step, the adsorbed CH_3O binds to Mn through O with an adsorption energy of -455.20 KJ/mol. Subsequently, the formed CH_2O adsorbs on the Mn-Cu site with O and C anchoring to Mn and Cu, respectively. In addition, the adsorption energy of CH_2O is -270.03 KJ/mol. Subsequently, the CH_2O is prone to further dehydrogenation. After the TS15, the CHO and H are generated. This step is endothermic by 60.76 KJ/mol with an activation energy of 93.55 KJ/mol. Finally, the CO is formed from the CHO dehydrogenation through TS16. In this step, the CHO adsorbs on Mn via C with an adsorption energy of -370.33 KJ/mol, and the corresponding activation energy and reaction energy are 53.04 KJ/mol and -81.01 KJ/mol, respectively.

3.2.5 Un-doped H_2O/Cu(110)

In order to compare with the results of on the metal (Pt, Pd, Ni, Mn) doped H_2O/Cu(110) surfaces, we also investigate the CH_3OH decomposition on the

un-doped H_2O/Cu(110) surface. The potential energy diagram with the optimal pathway is shown in Fig.7. Based on the energetic data from our calculation, CH_3OH adsorbs on the top site through O with an adsorption energy of -47.26 KJ/mol, and the dissociation of CH_3OH via the O-H bond scission give rise to the chemisorbed CH_3O and H through TS17. The reaction $CH_3OH \rightarrow CH_3O+H$ is exothermic by -14.47 KJ/mol with an activation energy of 41.47 KJ/mol. By contrast, the CH_2OH formation needs to overcome a barrier of 167.81 KJ/mol, which is higher than that of the CH_3O formation (41.47 KJ/mol), (see Fig.S1). Therefore, the CH_3O formation is easy to happen. The CH_3O intermediate leads to CH_2O through TS18. In this step, the CH_3O binds to the short-bridge site through O with an adsorption energy of -307.64 KJ/mol. The calculated activation energy is 112.83 KJ/mol, and the reaction energy is 91.62 KJ/mol. Subsequently, the CH_2O dehydrogenate to CHO via TS19. This step starts from the adsorbed CH_2O, where binds to the hollow site with C and O anchoring to the Cu, and the corresponding adsorption energy is -58.83 KJ/mol. The activation energy is 91.62 KJ/mol with endothermic by 19.29 KJ/mol. Finally, the adsorbed CHO coordinates to the top site via C with an adsorption energy of -224.71 KJ/mol, and CO is produced through TS20. The reaction $CHO \rightarrow CO+H$ requires an activation energy of 11.57 KJ/mol with exothermicity of -44.36 KJ/mol.

3.3. General Discussion

In this section, a detailed comparison of CH_3OH decomposition on the metal (Pt, Pd, Ni, Mn) doped and un-doped H_2O/Cu(110) surfaces are presented. Obviously, the introduction of metal (Pt, Pd, Ni, Mn) affects the adsorption energies of all the

adsorbates. On the un-doped H_2O/Cu(110) surface, CH_2O is easy to desorb instead of being further dehydrogenated due to the lower desorption energy than the activation energy of CHO formation (58.83 vs 91.62 KJ/mol), which is in consistence with the experimental observation [58, 59]. Interestingly, the introduction of metal (Pt, Pd, Ni, Mn) into H_2O/Cu(110) surface increase the bonding strength of CH_2O, which effectively hinders the CH_2O desorption (85.83 vs 50.15 KJ/mol, 82.94 vs 39.54 KJ/mol, 130.19 vs 62.69 KJ/mol, 270.03 vs 93.55 KJ/mol). Comparing with the results of CH_3OH dehydrogenation on the un-doped H_2O/Cu(110) surface, it is easy to find that the doping metal (Pt, Pd, Ni, Mn) on the H_2O/Cu(110) surface remarkably affect the reaction energies and activation energies of the main steps during CH_3OH decomposition processes.

For un-doped H_2O/Cu(110), the sequential dehydrogenation of CH_3OH to form CH_3O (41.47 KJ/mol activation energy), CH_2O (112.83 KJ/mol activation energy), CHO (91.62 KJ/mol activation energy) and CO (11.57 KJ/mol activation energy) is calculated. The rate-limiting step is the CH_3O dehydrogenation to CH_2O with a high activation energy (112.83 KJ/mol), which is in consistence with the previous DFT reported [12, 13]. For the Pt and Pd metals doped H_2O/Cu(110), as shown in Fig.3 and Fig.4, the activation energies for CH_3O formation are 43.40 and 19.29 KJ/mol, respectively, and both reactions are easy to occur. More importantly, compared to that of on the un-doped H_2O/Cu(110) surface, the activation energies for CH_3O dehydrogenation are significantly reduced (49.18 vs 112.83 KJ/mol, 41.47 vs 112.83 KJ/mol). The CHO formation is relatively easy on both Pt and Pd metals doped

H_2O/Cu(110) with the activation energies of 50.15 and 39.54 KJ/mol, respectively. The rate-limiting step is the CO formation from CHO dissociation, and the corresponding activation energies are 60.76 and 57.86 KJ/mol, respectively. Overall, the Pt and Pd dopants are favorable for the hydrogen formation from CH_3OH decomposition. For the CH_3OH decomposition on the Ni-doped H_2O/Cu(110), the activation energy of CH_3O formation is 92.58 KJ/mol, which is significantly higher than that on the un-doped H_2O/Cu(110) surface (41.47 KJ/mol), indicating that Ni dopant hinder the O-H bond scission of CH_3OH to some extent. The CH_2O formation is the rate-limiting step with an activation energy of 103.19 KJ/mol, which is lower than that of the un-doped H_2O/Cu(110) surface (112.83 KJ/mol). Subsequently, the sequential dehydrogenation of CH_2O to form CHO (62.69 KJ/mol activation energy) and CO (27.00 KJ/mol activation energy) are easy to occur. Therefore, the hydrogen formation from CH_3OH decomposition is also facilitated by the Ni dopant, which is similar to the previous experimental observation [26]. For the Mn-doped H_2O/Cu(110), as shown in Fig.6, the activation energies of the successive dehydrogenation of CH_3OH ($CH_3OH \rightarrow CH_3O \rightarrow CH_2O \rightarrow CHO \rightarrow CO$) are 26.04, 123.44, 93.55 and 53.04 KJ/mol. The rate-limiting step is also the CH_2O formation with an activation energy of 123.44 KJ/mol, which is higher than that on the un-doped H_2O/Cu(110) surface (112.83 KJ/mol). From the perspective of kinetics, the Mn doped H_2O/Cu(110) surface is slightly unfavorable for the CH_3OH dehydrogenation.

In summary, the sequential dehydrogenation of CH_3OH ($CH_3OH \rightarrow CH_3O \rightarrow CH_2O \rightarrow CHO \rightarrow CO$) on the metal (Pt, Pd, Ni, Mn) doped and un-doped H_2O/Cu(110) are

calculated and compared. Among all the metals doped H_2O/Cu(110) surfaces, the catalytic activity sequence for CH_3OH dehydrogenation is as follows: Pd-H_2O/Cu(110) > Pt-H_2O/Cu(110) > Ni-H_2O/Cu(110) > H_2O/Cu(110) > Mn-H_2O/Cu(110). Therefore, the metal dopants on the H_2O/Cu(110) surface play a significant role in CH_3OH decomposition reaction.

3.3.1 Electronic properties

In order to further clarify the influence of the dopants to local electronic structure of catalyst, the corresponding total density of states (DOS) and partial density of states (PDOS) of metal (Pt, Pd, Ni, Mn) doped H_2O/Cu(110) and un-doped H_2O/Cu(110) are investigated. As shown in the supporting information of Fig.S2, from the DOS, the energy gap exist from -21.00 eV to -10.50 eV for all the metal doped and un-doped H_2O/Cu(110) catalysts. Meanwhile, it is easy to find that the large and prominent peaks in DOS calculation mainly drive from Cu-3d state contribution. The low peaks in DOS from -22.20 eV to -21.00 eV and -10.50 eV to -9.00 eV are mainly drive from O-2s and O-2p state contribution, respectively.

To our knowledge, the electron distribution difference between metal dopants and neighboring copper atoms may causes the local electronic structure distortion, and then, changing the chemical and physical properties of catalysts. As shown in Fig.8 (a-e), comparing the PDOS curves, we can find that there exist a significant orbitals hybridization between Pt, Pd and Cu due to a large orbitals overlap of Pt 5d, Pd 4d orbital with Cu 3d orbital, respectively. There have a relative small orbital overlap between Ni and Cu, indicating that a relatively weakly hybridization of Ni 3d orbital

and Cu 3d orbital. Therefore, the local electronic distribution is changed effectively, especially for Pt and Pd metal dopants. This change may facilitate the catalytic reaction. In addition, slight orbital overlap between Mn 3d and Cu 3d is observed, which may not have a positive influence on catalytic reaction.

3.3.2 Kinetic-Thermodynamic Relationships

The kinetic and thermodynamic relationship is put forward by Brønsted [60], Evans and Polanyi [61](BEP), and the BEP relationship is reintroduced into the DFT framework by Neurock [62] and Nørskov [63]. Recently, BEP correlations are reported for the dissociation reactions, such as the diatomic molecules bond scission [63], the ethanol dissociation [64], the water-gas shift reaction [65-67] and the methanol decomposition and reverse reaction [55]. The BEP relationship is combined with linear scaling relations to estimate activation energy by the reaction energy changes of the elementary reaction on the corresponding catalytic processes without calculating the corresponding transition states, which saves computational cost to some extent.

Fig.9 shows the BEP plot for the CH_3OH dissociation steps associated with the main reaction route including O-H and C-H bond activation studied on the metal (Pt, Pd, Ni, Mn) doped and un-doped H_2O/Cu(110) surfaces. In this work, good BEP correlation means that the activation energies increase with the increase of reaction energies for the CH_3OH dehydrogenation elementary steps. In other word, the more the exothermic of the reaction is, the lower the corresponding activation energy will be. The slope of the identified BEP relationship are greater than 0.7, which means that surface decomposition reactions approach to product-like or late barrier.

4. Conclusions

In this paper, the periodic and self-consistent DFT calculations are performed to systematically investigate the effect of metal dopants on the H_2O/Cu(110) surface for CH_3OH decomposition reaction. The sequential dehydrogenation steps of CH_3OH ($CH_3OH \rightarrow CH_3O \rightarrow CH_2O \rightarrow CHO \rightarrow CO$) is studied. The result show that the introduction of metal (Pt, Pd, Ni, Mn) on the H_2O/Cu(110) surface notably influence the adsorption configurations and adsorption energies of all the adsorbates, and remarkably affect the reaction energies and activation energies of the elementary steps. The metal dopants are effectively hinder the by-product of CH_2O desorption. Overall, the Pt, Pd and Ni dopants are able to promote the hydrogen formation from CH_3OH decomposition, while Mn doped is unfavorable for the reaction. The CH_3OH decomposition catalytic activity is found to decrease in the sequence: Pd-H_2O/Cu(110) > Pt-H_2O/Cu(110) > Ni-H_2O/Cu(110) > H_2O/Cu(110) > Mn-H_2O/Cu(110).

On the basic of the main CH_3OH decomposition pathway, the Brønsted - Evans - Polanyi plot for the CH_3OH dehydrogenation steps on the metal (Pt, Pd, Ni, Mn) doped and un-doped H_2O/Cu(110) surfaces is identified, and a linear relationship between all reaction energies and transition state energies are presented. Finally, our study may be useful for the designing of novel Cu-based catalysis for CH_3OH decomposition on the liquid/solid interface.

Acknowledgments

The authors gratefully acknowledge the financial support of this study by the

National Natural Science Foundation of China (21406154), Natural Science Foundation of Shanxi (2013021007-5), Special/Youth Foundation of Taiyuan University of Technology (2012L041 and 2013T092). The authors especially thank anonymous reviewers for their helpful suggestions.

References

1. N. Abas, A. Kalair and N. Khan, *Futures.*, 2015, **69**, 31-49.
2. X. Zhang, S. H. Chan, H. K. Ho, S.-C. Tan, M. Li, G. Li, J. Li and Z. Feng, *Int. J. Hydrogen Energy.*, 2015, **40**, 6866-6919.
3. D. Cebrucean, V. Cebrucean and I. Ionel, *Energy Procedia.*, 2014, **63**, 18-26.
4. B. Barrett, J. W. Charles and J. L. Temte, *Prev. Med.*, 2015, **70**, 69-75.
5. D. Ross, *Vacuum*, 2006, **80**, 1084-1089.
6. S. K. Kamarudin, W. R. W. Daud, Z. Yaakub, Z. Misron, W. Anuar and N. Yusuf, *Int. J. Hydrogen Energy.*, 2009, **34**, 2077-2088.
7. L. Mingyi, Y. Bo, X. Jingming and C. Jing, *J. Power Sources.*, 2008, **177**, 493-499.
8. S. Sá, H. Silva, L. Brandão, J. M. Sousa and A. Mendes, *Appl. Catal. B-Environ.*, 2010, **99**, 43-57.
9. G. A. Olah, *Angew. Chem. Int. Ed.*, 2005, **44**, 2636-2639.
10. D. R. Palo, R. A. Dagle and J. D. Holladay, *Chem.Rev.*, 2007, **107**, 3992-4021.
11. C. N. Hamelinck and A. P. Faaij, *J. Power Sources.*, 2002, **111**, 1-22.
12. D. Mei, L. Xu and G. Henkelman, *J. Phys. Chem. C.*, 2009, **113**, 4522-4537.
13. Z.-J. Zuo, L. Wang, P.-D. Han and W. Huang, *Int. J. Hydrogen Energy.*, 2014, **39**, 1664-1679.
14. J. G. M. Mavrikakis, *J. Am. Chem. Soc.*, 2004, **126**, 3910-3919.
15. J. Agrell, M. Boutonnet and J. L. G. Fierro, *Appl. Catal. A-Gen.*, 2003, **253**, 213-223.
16. H. Kobayashi, N. Takezawa and C. Minochi, *J. Catal.*, 1981, **69**, 487-494.
17. C. Jiang, D. Trimm, M. Wainwright and N. Cant, *Appl. Catal. A-Gen.*, 1993,

97, 145-158.

18. T. Tsoncheva, I. Genova, M. Dimitrov, E. Sarcadi-Priboczki, A. M. Venezia, D. Kovacheva, N. Scotti and V. dal Santo, *Appl. Catal. B-Environ.*, 2015, **165**, 599-610.
19. Z. C. Kramer, X.-K. Gu, D. D. Y. Zhou, W.-X. Li and R. T. Skodje, *J. Phys. Chem. C.*, 2014, **118**, 12364-12383.
20. Y. Sakata, K. Domen, K.-i. Maruya and T. Onishi, *Appl. Surf. Sci.*, 1989, **35**, 363-370.
21. C.-Q. Lv, J.-H. Liu, H. Wang and G.-C. Wang, *Catal. Commun.*, 2015, **60**, 60-64.
22. S. Sakong and A. Gross, *J. Phys. Chem. A*., 2007, **111**, 8814-8822.
23. C. Zhang, Z. Yuan, N. Liu, S. Wang and S. Wang, *Fuel Cells.*, 2006, **6**, 466-471.
24. P. Mierczynski, K. Vasilev, A. Mierczynska, W. Maniukiewicz and T. P. Maniecki, *Appl. Catal. A- Gen.*, 2014, **479**, 26–34.
25. H. C. D. Jongste, V. Ponec and F. G. Gault, *J. Catal.*, 1980, **63**, 395–403.
26. J. Xi, Z. Wang and G. Lu, *Appl. Catal. A-Gen.*, 2002, **225**, 77-86.
27. F. Studt, F. Abild-Pedersen, Q. Wu, A. D. Jensen, B. Temel, J.-D. Grunwaldt and J. K. Nørskov, *J. Catal.*, 2012, **293**, 51-60.
28. R. Pérez-Hernández, G. M. Galicia, D. M. Anaya, J. Palacios, C. Angeles-Chavez and J. Arenas-Alatorre, *Int. J. Hydrogen Energy.*, 2008, **33**, 4569-4576.
29. M. R. Morales, B. P. Barbero and L. E. Cadús, *Appl. Catal. B-Environ.*, 2006, **67**, 229-236.
30. H. Borchert, B. Jurgens, T. Nowitzki, P. Behrend, Y. Borchert, V. Zielasek, S. Giorgio, C. Henry and M. Baumer, *J. Catal.*, 2008, **256**, 24-36.
31. Y.-D. Li, T.-W. Liao, C.-X. Wang, C.-S. Chao, T.-C. Hung, C. Ho, M.-F. Luo, Y.-L. Lai and Y.-J. Hsu, *RSC Adv.*, 2014, **4**, 31602-31613.
32. M. Michalska-Domańska, M. Norek, P. Jóźwik, B. Jankiewicz, W. J. Stępniowski and Z. Bojar, *Appl. Surf. Sci.*, 2014, **293**, 169-176.

33. P. Mierczynski, K. Vasilev, A. Mierczynska, W. Maniukiewicz and T. P. Maniecki, *Appl. Catal. A-Gen.*, 2014, **479**, 26-34.
34. R. Pérez-Hernández, G. Mondragón Galicia, D. Mendoza Anaya, J. Palacios, C. Angeles-Chavez and J. Arenas-Alatorre, *Int. J. Hydrogen Energy.*, 2008, **33**, 4569-4576.
35. T. Fukunaga, N. Ryumon, N. Ichikuni and S. Shimazu, *Catal. Commun.*, 2009, **10**, 1800-1803.
36. J. Papavasiliou, G. Avgouropoulos and T. Ioannides, *J. Catal.*, 2007, **251**, 7-20.
37. R. Razzaq, H. Zhu, L. Jiang, U. Muhammad, C. Li and S. Zhang, *Ind. Eng. Chem. Res.*, 2013, **52**, 2247-2256
38. B. S. Akpa, C. D'Agostino, L. F. Gladden, K. Hindle, H. Manyar, J. McGregor, R. Li, M. Neurock, N. Sinha, E. H. Stitt, D. Weber, J. A. Zeitler and D. W. Rooney, *J. Catal.*, 2012, **289**, 30-41.
39. J. Liu, X.-M. Cao and P. Hu, *Phys. Chem. Chem. Phys.*, 2014, **16**, 4176-4185.
40. D. Tongsakul, S. Nishimura and K. Ebitani, *J. Phys. Chem. C.*, 2014, **118**, 11723-11730.
41. H.-F. Wang and Z.-P. Liu, *J. Phys. Chem. C.*, 2009, **113**, 17502-17508.
42. Y.-H. Fang and Z.-P. Liu, *Surf. Sci.*, 2015, **631**, 42-47.
43. Y. Okamoto, O. Sugino, Y. Mochizuki, T. Ikeshoji and Y. Morikawa, *Chem. Phys. Lett.*, 2003, **377**, 236-242.
44. P. Ordejón, E. Artacho and J. M. Soler, *Phys. Rev. B.*, 1996, **53**, R10441.
45. L. Grabow and M. Mavrikakis, *ACS Catal.*, 2011, **1**, 365-384.
46. G. Kresse and J. Furthmüller, *Phys. Rev. B.*, 1996, **54**, 11169.
47. G. Kresse and J. Furthmüller, *Comput. Mater. Sci.*, 1996, **6**, 15-50.
48. G. Kresse and D. Joubert, *Phys. Rev. B.*, 1999, **59**, 1758.
49. J. P. Perdew and Y. Wang, *Phys. Rev. B.*, 1992, **45**, 13244-13249.
50. J. P. Perdew, K. Burke and M. Ernzerhof, *Phys. Rev. Lett*., 1996, **77**, 3865.
51. M. Methfessel and A. Paxton, *Phys. Rev. B.*, 1989, **40**, 3616-3621.
52. D. Sheppard, P. Xiao, W. Chemelewski, D. D. Johnson and G. Henkelman, *J.*

Chem. Phys., 2012, **136**, 074103.

53. Y. Fang and Z. Liu, *Sci. China Chem.*, 2010, **53**, 543-552.
54. Z.-J. Zuo, L. Wang, P.-D. Han and W. Huang, *Comput. Theor. Chem.*, 2014, **1033**, 14-22.
55. R. García-Muelas, Q. Li and N. López, *ACS Catal.*, 2015, **5**, 1027-1036.
56. J. Greeley and M. Mavrikakis, *J. Catal.*, 2002, **208**, 291-300.
57. S. Lin, R. S. Johnson, G. K. Smith, D. Xie and H. Guo, *Phys. Chem. Chem. Phys.*, 2011, **13**, 9622-9631.
58. I. E. Wachs and R. J. Madix, *J. Catal.*, 1978, **53**, 208-227.
59. M. Bowker and R. Madix, *Surf. Sci.*, 1980, **95**, 190-206.
60. J. Bronsted, *Chem. Rev.*, 1928, **5**, 231-338.
61. M. Evans and M. Polanyi, *Trans. Faraday. Soci.*, 1938, **34**, 11-24.
62. V. Pallassana and M. Neurock, *J. Catal.*, 2000, **191**, 301-317.
63. J. K. Nørskov, T. Bligaard, A. Logadottir, S. Bahn, L. B. Hansen, M. Bollinger, H. Bengaard, B. Hammer, Z. Sljivancanin and M. Mavrikakis, *J. Catal.*, 2002, **209**, 275-278.
64. R. Alcala, M. Mavrikakis and J. A. Dumesic, *J. Catal.*, 2003, **218**, 178-190.
65. R. C. Catapan, A. A. Oliveira, Y. Chen and D. G. Vlachos, *J. Phys. Chem. C.*, 2012, **116**, 20281-20291.
66. S.-C. Huang, C.-H. Lin and J.-H. Wang, *J. Phys. Chem. C.*, 2010, **114**, 9826-9834.
67. J. Jelic and R. J. Meyer, *J. Catal.*, 2010, **272**, 151-157.

Figure caption

Fig.1 The top view surface configuration of the H_2O/Cu(110) surface: (a) metal (Pt, Pd, Ni, Mn) doped; (b) un-doped.

Fig.2 The configurations of the reaction intermediates involved in methanol decomposition on the metal (Pt, Pd, Ni, Mn) doped and un-doped H_2O/Cu(110) surfaces (The Cu, Pt, Pd, Ni, Mn, C, O and H atoms are shown in the brown, deep blue, dark green, wathet blue, purple, gray, red, and white balls, respectively).

Fig.3 Potential energy profile of the main route for CH_3OH decomposition on the Pt doped H_2O/Cu(110) surface.

Fig.4 Potential energy profile of the main route for CH_3OH decomposition on the Pd doped H_2O/Cu(110) surface.

Fig.5 Potential energy profile of the main route for CH_3OH decomposition on the metal Ni doped H_2O/Cu(110) surface.

Fig.6 Potential energy profile of the main route for CH_3OH decomposition on the Mn doped H_2O/Cu(110) surface.

Fig.7 Potential energy profile of the main route for CH_3OH decomposition on the un-doped H_2O/Cu(110) surface.

Fig.8. The partial density of states (PDOS) for metal (Pt, Pd, Ni, Mn) doped H_2O/Cu(110) (a, b, c and d) and un-doped H_2O/Cu(110) (e). The insets are the PDOS of the metal dopants and neighboring copper atom.

Fig.9. Brønsted-Evans-Polanyi plots of the calculated transition state energy (E-TS) versus final state energy (E-FS) for the main route of CH_3OH decomposition on the metal (Pt, Pd, Ni, Mn) doped and un-doped H_2O/Cu(110) surfaces. The reactant energy in vacuum as a reference to calculate the transition and final state energies of each elementary reaction.

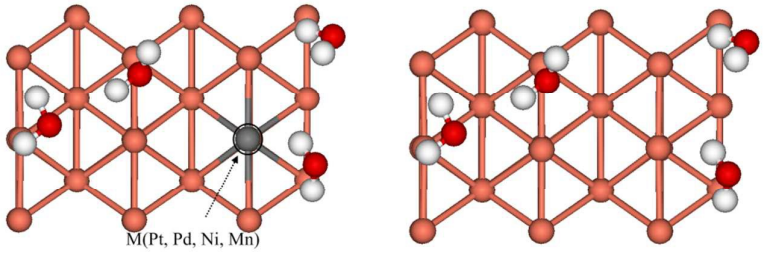

Fig.1 The top view surface configuration of the H_2O/Cu(110) surface: (a) metal (Pt, Pd, Ni, Mn) doped; (b) un-doped.

(Pt-doped H_2O/Cu(110) surface)

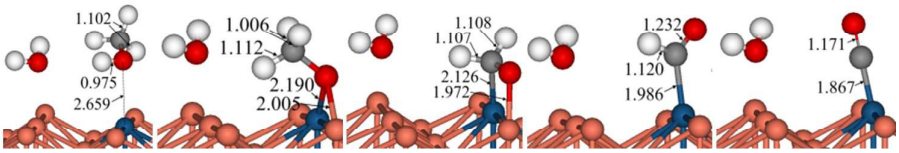

CH_3OH* **CH_3O*** **CH_2O*** **CHO*** **CO***

(Pd-doped H_2O/Cu(110) surface)

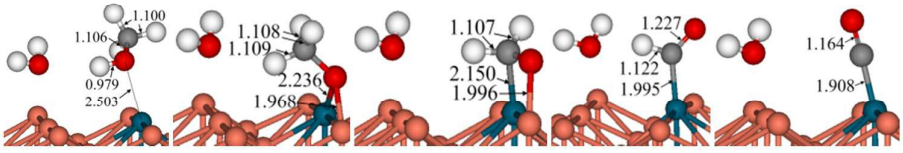

CH_3OH* **CH_3O*** **CH_2O*** **CHO*** **CO***

(Ni-doped H_2O/Cu(110) surface)

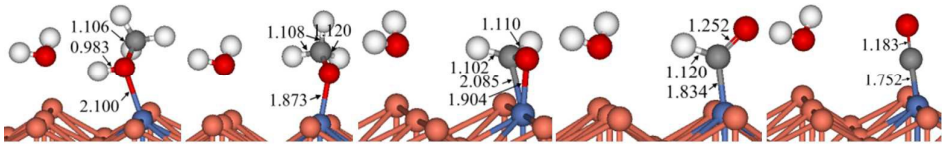

CH_3OH* **CH_3O*** **CH_2O*** **CHO*** **CO***

(Mn-doped H_2O/Cu(110) surface)

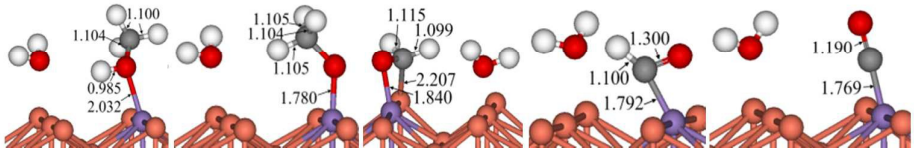

CH_3OH* **CH_3O*** **CH_2O*** **CHO*** **CO***

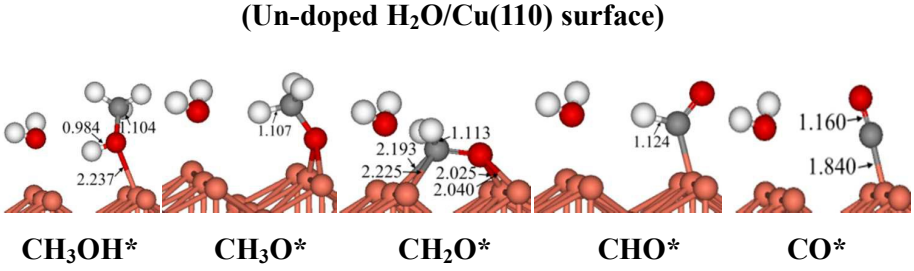

Fig.2 The configurations of the reaction intermediates involved in methanol decomposition on the metal (Pt, Pd, Ni, Mn) doped and un-doped H_2O/Cu(110) surfaces (The Cu, Pt, Pd, Ni, Mn, C, O and H atoms are shown in the brown, deep blue, dark green, wathet blue, purple, gray, red, and white balls, respectively).

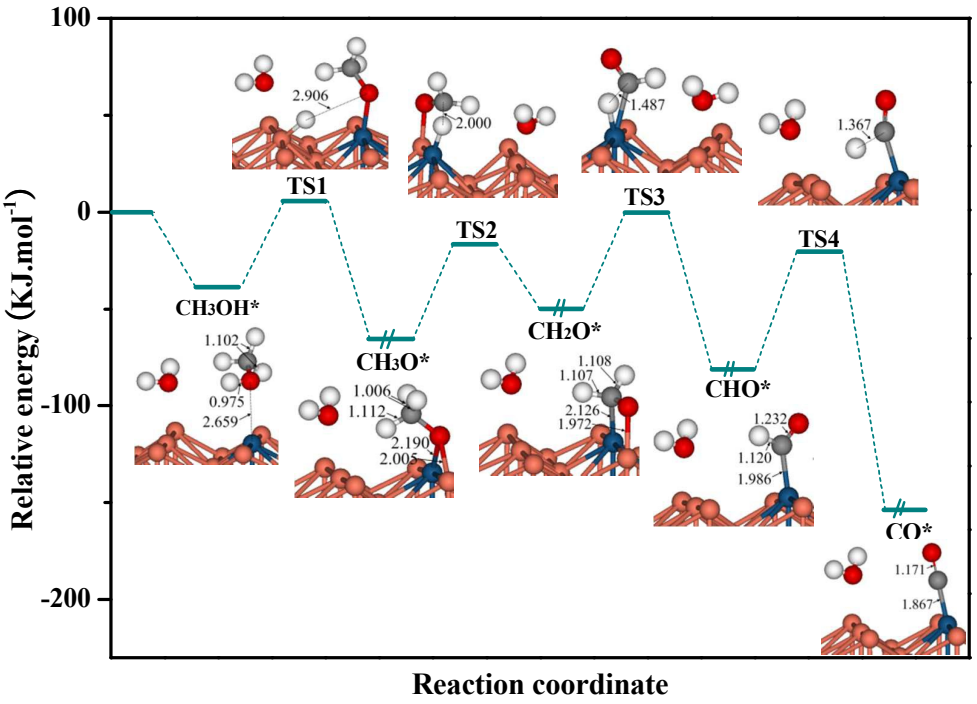

Fig.3 Potential energy profile of the main route for CH_3OH decomposition on the Pt doped H_2O/Cu(110) surface.

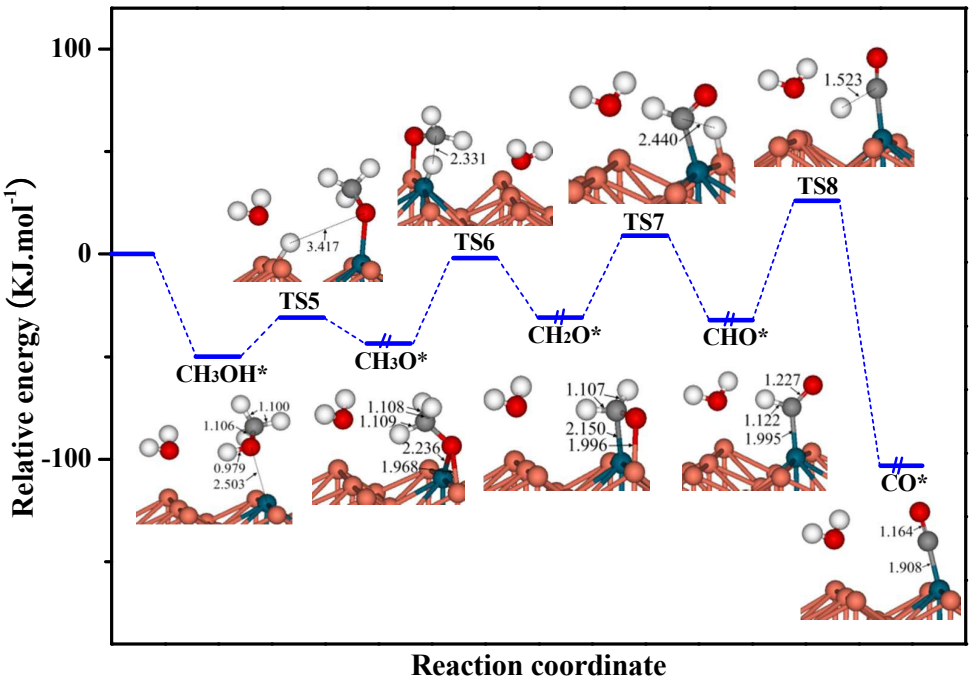

Fig.4 Potential energy profile of the main route for CH_3OH decomposition on the Pd doped H_2O/Cu(110) surface.

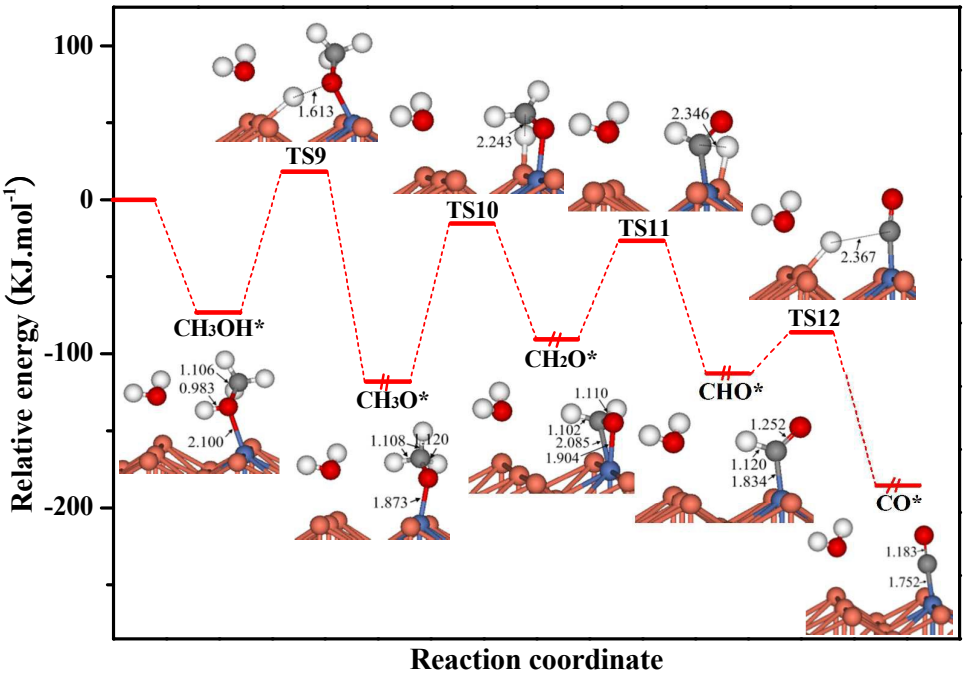

Fig.5 Potential energy profile of the main route for CH_3OH decomposition on the metal Ni doped H_2O/Cu(110) surface.

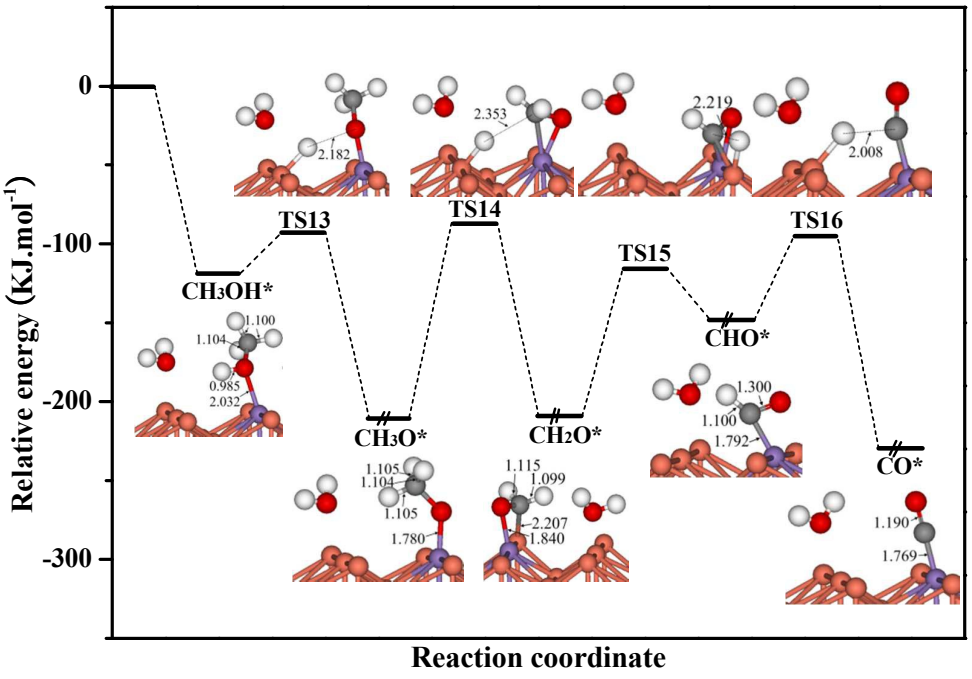

Fig.6 Potential energy profile of the main route for CH_3OH decomposition on the Mn doped H_2O/Cu(110) surface.

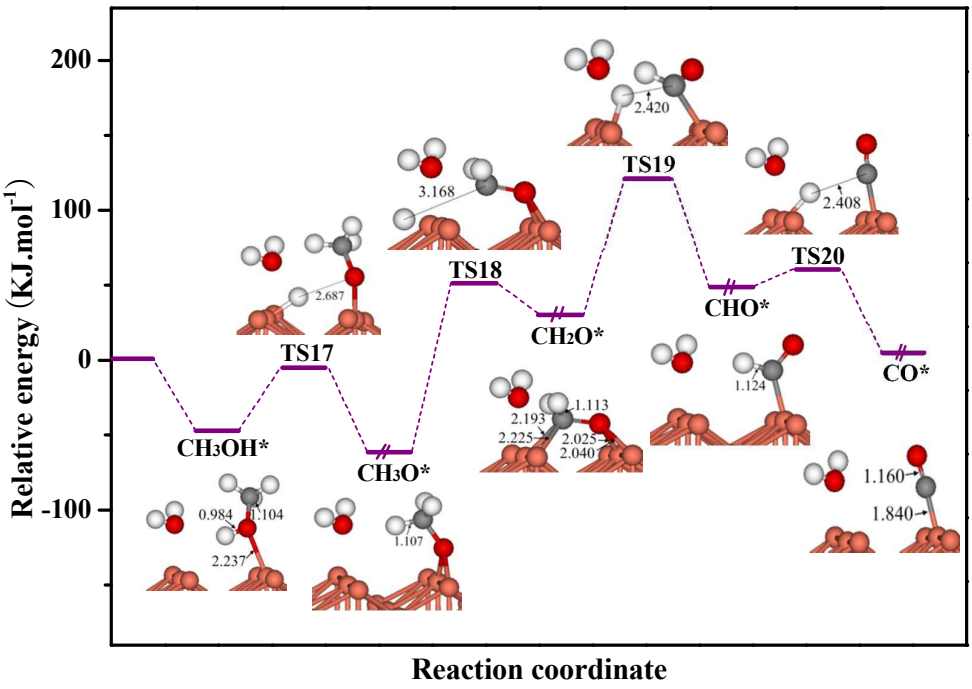

Fig.7 Potential energy profile of the main route for CH_3OH decomposition on the un-doped H_2O/Cu(110) surface.

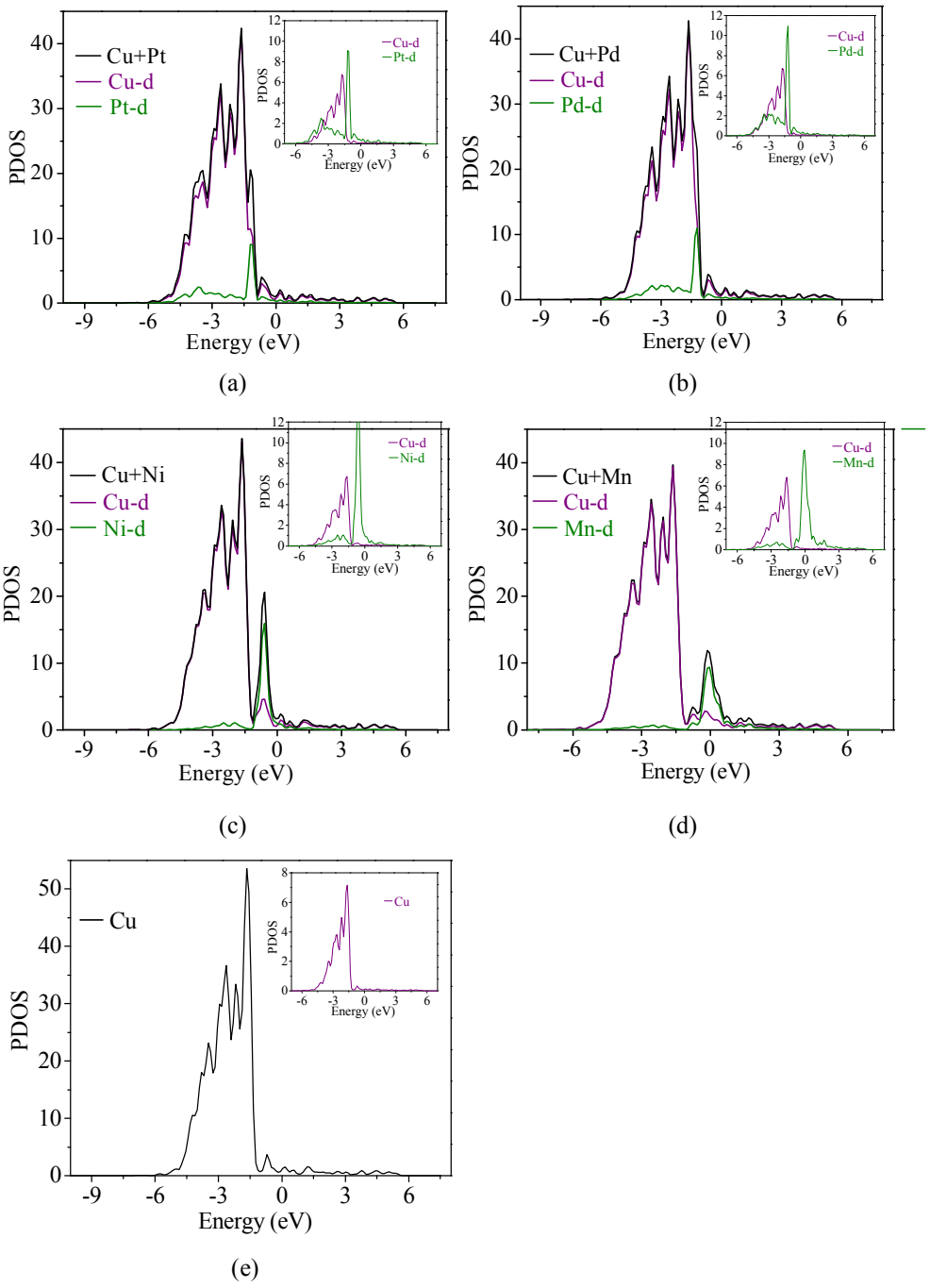

Fig.8. The partial density of states (PDOS) for metal (Pt, Pd, Ni, Mn) doped H_2O/Cu(110) (a, b, c and d) and un-doped H_2O/Cu(110) (e). The insets are the PDOS of the metal dopants and neighboring copper atom.

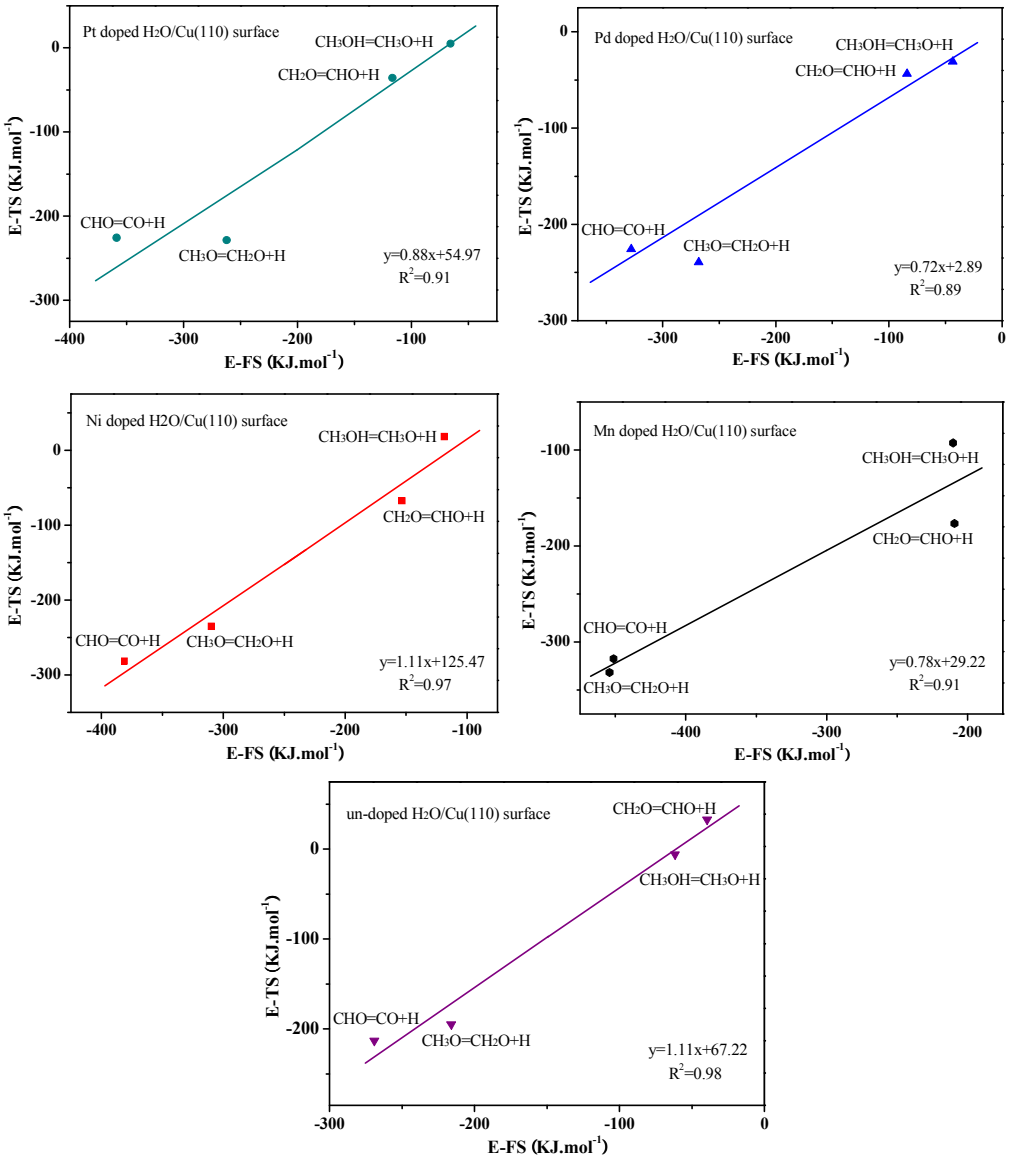

Fig.9. Brønsted-Evans-Polanyi plots of the calculated transition state energy (E-TS) versus final state energy (E-FS) for the main route of CH_3OH decomposition on the metal (Pt, Pd, Ni, Mn) doped and un-doped H_2O/Cu(110) surfaces. The reactant energy in vacuum as a reference to calculate the transition and final state energies of each elementary reaction.